Available online at www.sciencedirect.com

ScienceDirect

Advances in Space Research 74 (2024) 2302–2315

ADVANCES IN SPACE RESEARCH (a COSPAR publication)

www.elsevier.com/locate/asr

Distributed prescribed-time coordinated control of spacecraft formation flying under input saturation

Chuang Xu [a], Daniel Zelazo [b], Baolin Wu [c,*]

[a] Aerospace Time Feipeng Company Limited, Suzhou 215000, China
[b] Technion – Israel Institute of Technology, Haifa 3100000, Israel
[c] Harbin Institute of Technology, Harbin 150080, China

Received 2 February 2024; received in revised form 16 May 2024; accepted 31 May 2024
Available online 6 June 2024

Abstract

This paper studies the prescribed-time relative motion control problem of spacecraft formation flying under input saturation. Using prescribed-time theory, a prescribed-time sliding mode is designed such that the states on the sliding mode converge to the equilibrium in the prescribed time. Based on the prescribed-time sliding mode, a prescribed-time relative motion tracking controller is developed, which guarantees fast formation maneuvers with feasible fuel consumption and strong robustness under input saturation. Furthermore, a simulation example is carried out to verify the effectiveness of the proposed controller.

Keywords: Spacecraft formation flying; Distributed control; Prescribed-time control; Input saturation

1. Introduction

Spacecraft formation flying (SFF) has attracted much attention for its diverse applications in many space missions, such as, synthetic aperture radar interferometry (Rosen et al., 2000) and terrestrial planet finding (Lawson, 2001). Compared with a monolithic spacecraft, SFF has the advantages of added robustness, lower cost, and higher feasibility (Hu and Shi, 2020). In general, relative motion control methods for SFF can be classified into two main types: impulsive control and continuous control. The impulsive control methods use chemical thrusters and generate control commands to match the instantaneous orbital elements to the desired orbital elements (Schaub et al., 2000; Pini Gurfil, 2007). In the past decades, the impulsive control methods are mainly based on the Cartesian relative spacecraft position components (Gurfil, 2005) or hybrid classical elements-relative position feedback (Schaub and Alfriend, 2002). Chernick and D'Amico (2021) proposed an optimal impulsive control method to achieve spacecraft relative orbit reconfiguration by using reachable set theory. Continuous control methods rely on low-thrust electric propulsion and can maintain small steady-state errors under orbital perturbations. In light of this, numerous results using continuous control of SFF have appeared in recent years (Zhang and Song, 2012; Lee et al., 2015; Hu et al., 2015; Sun et al., 2018; Di Mauro et al., 2019; Huang and Jia, 2019; Hu and Shi, 2020). Sun et al. (2018) proposed a neural-network-based spacecraft formation control law using aerodynamics forces.

However, the above-mentioned results can only ensure asymptotic stability of SFF system. To achieve faster

* Corresponding author.
E-mail address: wuba0001@e.ntu.edu.sg (B. Wu).

https://doi.org/10.1016/j.asr.2024.05.077

convergence rates and better robustness, finite-time control methods (FTCM) and fixed-time control methods (DTCM) have been developed. FTCM guarantees that system states converge to the equilibrium in a finite time dependent on the initial system states, while DTCM guarantees that system states converge to the equilibrium in a finite time independent on the initial system states. Thus, DTCM can be regarded as an extension of FTCM. Wang et al. in (Wang et al., 2012) proposed a finite-time controller for SFF by using dual-quaternion. Hu et al. in (Hu and Zhang, 2015) studied finite-time attitude coordinated control for SFF subjected to input saturation. Ran et al. in (Ran et al., 2017) proposed two finite-time convergent coordinated formation controllers for SFF under directed communication topology. In (Zhuang et al., 2021a), a fixed-time coordinated tracking control was employed for SFF to avoid collision.

It should be pointed out that the upper-bound of convergence time of DTCM is calculated by control parameters. It is not easy to choose these parameters when the upper-bound for the convergence time is given. Furthermore, the upper-bound time is very conservative and not the least upper-bound for the convergence time. To deal with these problems, the prescribed-time control method (PTCM) is developed, where the upper-bound of convergence time is designed by users and the user-designed time is the least upper-bound of convergence time. In light of this, some results in the field of multi-agent systems (Anguiano-Gijón et al., 2019; Wang et al., 2018; Chen et al., 2020; Ma et al., 2023), attitude control for spacecraft (Xiao et al., 2021; Xie et al., 2022) and attitude consensus control for SSF (Xu et al., 2021b; Xu et al., 2021a) have been presented. The results in (Xu et al., 2021b; Xu et al., 2021a) deal with the attitude consensus problem, but do not solve the relative motion control problem. In attitude consensus, the spacecraft collaborate with each other to align only their attitude, while the relative motion control problem aims to control the positions of the spacecraft relative to each other. In this regard, attitude consensus and relative motion control require different control strategies. The attitude consensus strategies can not be directly applied to relative motion control problem. To the best of our knowledge, there are few works about the prescribed-time stability for the relative motion control problem of SFF. Furthermore, low-thrust electric propulsion has been used in many space missions (such as deep space exploration and station-keeping for constellations) due to its high specific impulse and high maneuverability. However, low-thrust electric propulsion used in continuous control of SFF can only provide limited control force. Thus, it is necessary to take the control input saturation into consideration.

Motivated by the above discussion, we study the prescribed-time relative motion control problem of SFF under input saturation. Under the mild assumption that the relative sensor topology contains a directed spanning tree, we develop a novel prescribed-time sliding mode control. Compared with linear sliding mode or terminal sliding mode, the proposed sliding mode enables the states on the sliding mode to converge to the equilibrium in a user-specified finite-time. Then, based on the prescribed-time sliding mode, a distributed prescribed-time relative motion controller is proposed to enable relative motion coordinated tracking in a user-specified finite-time. In contrast to fixed-time spacecraft formation control method in Zhuang et al. (2021a), the proposed controller is distributed and uses the inter-spacecraft relative measurements to achieve the formation control such that only a subset of spacecraft in the formation need to measure the relative position and velocity with respect to (w.r.t.) the reference spacecraft. Furthermore, the upper-bound of convergence time is designed by users and more accurate in the proposed control scheme. The proposed controller also takes the control input saturation into consideration, and a rigorous proof is presented to verify that the tracking errors of the system states converge to a bounded region in a prescribed time under the saturation controller. Finally, we carry out a simulation to verify the effectiveness of the proposed controller.

Notions: a_r = semimajor axis of reference spacecraft, e_r = eccentricity of reference spacecraft, i_r = inclination of reference spacecraft, ω_r = argument of periapsis of reference spacecraft, Ω_r = longitude of the ascending node of reference spacecraft, θ_r = true anomaly of reference spacecraft, F_c = local-vertical local horizon (LVLH) frame, F_I = Earth centered inertial (ECI) frame, $\boldsymbol{r_i}$ = position of spacecraft i in ECI frame, $\boldsymbol{r_r}$ = position of reference spacecraft in ECI frame, $\boldsymbol{\rho}_i$ = position of spacecraft i in LVLH frame, $\boldsymbol{\rho}_i^{\star}$= desired position of spacecraft i in LVLH frame, $\tilde{\boldsymbol{\rho}}_i = \boldsymbol{\rho}_i - \boldsymbol{\rho}_i^{\star}$, $\boldsymbol{\rho}_{ij} = \boldsymbol{\rho}_i - \boldsymbol{\rho}_j$, $\boldsymbol{\rho}_{ij}^{\star} = \boldsymbol{\rho}_i^{\star} - \boldsymbol{\rho}_j^{\star}$, $\tilde{\boldsymbol{\rho}}_{ij} = \boldsymbol{\rho}_{ij} - \boldsymbol{\rho}_{ij}^{\star}$, n_r= mean angular velocity of reference spacecraft, μ= gravitational constant of Earth, m_i= mass of spacecraft i, $\mathbb{R}^+$= set of positive real number, $(\bullet)_r$ = value for reference spacecraft, $(\bullet)_i$ = value for spacecraft i, $(\bullet)_{ij}$ = value for spacecraft i with respect to spacecraft j.

2. Preliminaries

In this section, we provide some basic preliminaries from coordinate frames, spacecraft relative motion dynamical systems and graph theory that will be needed for this work.

2.1. Coordinate frames

As shown in Fig. 1, two frames, namely the *local-vertical local horizon* (LVLH) frame $F_c = \{x_c, y_c, z_c\}$ and the *Earth Centered Inertial* (ECI) frame $F_I = \{x_I, y_I, z_I\}$, are introduced to describe the motion of spacecraft in this paper. The origins of ECI and LVLH frames are set on the Earth center and a reference (leader) spacecraft, respectively. In the LVLH frames, the x_c axis points radially outward, the z_c axis points to the positive normal direction of the ref-

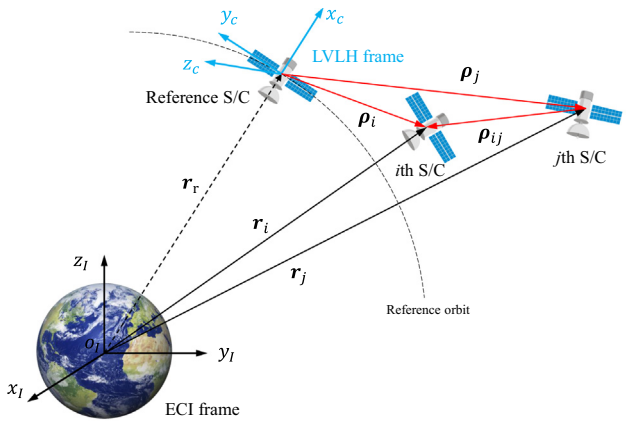

Fig. 1. Graphical description of the SFF system.

erence spacecraft orbit, and the y_c axis completes the setup to form a Cartesian coordinate frame in the x_c-y_c-z_c order.

2.2. Spacecraft dynamics

In this paper, the spacecraft formation consists of a reference (leader) spacecraft and n follower spacecrafts. All follower spacecraft need to maintain their relative motion with respect to the reference spacecraft. We define $\rho_i = [x_i, y_i, z_i]^T$ as the relative position of the ith follower spacecraft, w.r.t., the reference spacecraft in the LVLH frame. The relative motion dynamics of the ith follower spacecraft, w.r.t., the reference spacecraft in LVLH frame are given by (Hu and Shi, 2020; Zhuang et al., 2021b)

$$m_i\ddot{\rho}_i + \boldsymbol{C}_i\dot{\rho}_i + \boldsymbol{D}_i\rho_i + \boldsymbol{n}_i = \Gamma(\boldsymbol{f}_i) + \boldsymbol{d}_i, \tag{1}$$

$$\boldsymbol{C}_i = 2m_i\begin{bmatrix} 0 & -\dot{\theta}_r & 0 \\ \dot{\theta}_r & 0 & 0 \\ 0 & 0 & 0 \end{bmatrix}, \tag{2}$$

$$\boldsymbol{D}_i = m_i\begin{bmatrix} \mu/\|\boldsymbol{r}_i\|^3 - \dot{\theta}_r^2 & -\ddot{\theta}_r & 0 \\ \ddot{\theta}_r & \mu/\|\boldsymbol{r}_i\|^3 - \dot{\theta}_r^2 & 0 \\ 0 & 0 & \mu/\|\boldsymbol{r}_i\|^3 \end{bmatrix}, \tag{3}$$

$$\boldsymbol{n}_i = \mu m_i\left[\|\boldsymbol{r}_r\|/\|\boldsymbol{r}_i\|^3 - 1/\|\boldsymbol{r}_r\|^2, 0, 0\right]^T, \tag{4}$$

where $\Gamma(\boldsymbol{f}_i) = \text{sat}(\boldsymbol{f}_i)$ is the applied control force, $\boldsymbol{f}_i = [f_{i,1}, f_{i,2}, f_{i,3}]^T \in \mathbb{R}^3$ is the command control force vector, $\text{sat}(f_{i,k}) = \text{sign}(f_{i,k}) \times \min\{|f_{i,k}|, f_M\}, k = 1, 2, 3$, with f_M being the maximum allowable force, and $\boldsymbol{d}_i \in \mathbb{R}^3$ is the external disturbance vector. The evolution of the true anomaly θ_r is given by (Hu and Shi, 2020)

$$\dot{\theta}_r = \frac{n_r(1 + e_r\cos(\theta_r))}{(1 - e_r^2)^{3/2}}, \tag{5}$$

$$\ddot{\theta}_r = \frac{-2n_r^2 e_r(1 + e_r\cos(\theta_r))^3\sin(\theta_r)}{(1 - e_r^2)^3}, \tag{6}$$

where $n_r = \sqrt{\mu/a_r^3}$ is the mean angular velocity of the reference spacecraft. Define $\boldsymbol{\rho}_i^{\star}$ as the desired relative position of the spacecraft i. Then, the relative position tracking error is defined as

$$\tilde{\boldsymbol{\rho}}_i = \boldsymbol{\rho}_i - \boldsymbol{\rho}_i^{\star}. \tag{7}$$

As is shown in Fig. 1, the relative position between spacecraft i and spacecraft j is defined as $\boldsymbol{\rho}_{ij} = \boldsymbol{\rho}_i - \boldsymbol{\rho}_j$. The corresponding desired relative position of $\boldsymbol{\rho}_{ij}$ is defined as $\boldsymbol{\rho}_{ij}^{\star} = \boldsymbol{\rho}_i^{\star} - \boldsymbol{\rho}_j^{\star}$. Then, the relative position tracking error is defined as

$$\tilde{\boldsymbol{\rho}}_{ij} = \boldsymbol{\rho}_{ij} - \boldsymbol{\rho}_{ij}^{\star}. \tag{8}$$

The position tracking error dynamics is defined as follows (Zhuang et al., 2021b).

$$m_i\ddot{\tilde{\rho}}_i + \boldsymbol{g}_i + m_i\ddot{\rho}_i^{\star} = \boldsymbol{f}_i + \boldsymbol{d}_i, \tag{9}$$

where $\boldsymbol{g}_i = \boldsymbol{C}_i\dot{\tilde{\boldsymbol{\rho}}}_i + \boldsymbol{D}_i\tilde{\rho}_i + \boldsymbol{C}_i\dot{\rho}_i^{\star} + \boldsymbol{D}_i\boldsymbol{\rho}_i^{\star} + \boldsymbol{n}_i$.

2.3. Graph theory

A digraph $G = \{V, E, A\}$ is utilized to describe the sensor network among follower spacecraft in this paper, where $V = \{1, 2, \ldots, n\}$ is the set of follower spacecraft, $E \subseteq V \times V$ denotes the set of edges, and $A = [a_{ij}] \in \mathbb{R}^{n\times n}$ represents the weighted adjacency matrix. The weighted parameter $a_{ij} > 0$ if the spacecraft i can measure the relative position $\boldsymbol{\rho}_{ij}$ and relative velocity $\dot{\boldsymbol{\rho}}_{ij}$, otherwise, $a_{ij} = 0$. The set $N_i \triangleq \{j \in V : (i, j) \in E\}$ denotes the set of neighbors of the spacecraft i. The Laplacian matrix $L = [l_{ij}]_{n\times n}$ of the digraph G is defined as $l_{ij} = \sum_{j=1, j\neq i}^{n} a_{ij}$ if $i = j$ and $l_{ij} = -a_{ij}$ if $i \neq j$.

Denote the reference spacecraft as the spacecraft 0. The weighted matrix $A_0 = \text{diag}\{a_{i0}\} \in \mathbb{R}^{n\times n}$ is a matrix with $a_{i0} > 0$ if the spacecraft i can measure the relative position $\boldsymbol{\rho}_i$ and relative velocity $\dot{\boldsymbol{\rho}}_i$, and $a_{i0} = 0$ otherwise. The digraph $\bar{G} = \{\bar{V}, \bar{E}\}$ is defined to describe the sensor network among the reference and follower spacecraft, where $\bar{V} = \{0, 1, \ldots, n\}$ and $\bar{E} \subseteq \bar{V} \times \bar{V}$.

Lemma 1 ((*Shang and Ye*, 2017)). If the digraph $\bar{G}$ has a directed spanning tree with the reference spacecraft being the root, then the matrix $H = L + A_0$ is a non-singular matrix.

2.4. Finite-time and prescribed-time stability

In this section, some definitions and lemmas related to finite-time stability theory are introduced to facilitate the design of the control scheme. Consider the system

$$\dot{\boldsymbol{x}}(t) = \boldsymbol{F}(\boldsymbol{x}(t)),\ \boldsymbol{x}(t) \in \mathbb{R}^n, \tag{10}$$

where $\boldsymbol{F} : \mathbb{R}^n \to \mathbb{R}^n$ is a nonlinear map and $\boldsymbol{F}(\boldsymbol{0}) = \boldsymbol{0}$. The time variable t is defined on the interval $[0, \infty)$.

Definition 1 (*Finite-Time Stable* (*Ni et al., 2017*)). The equilibrium of the system (10) is said to be globally *finite-time stable* if any solution $\boldsymbol{x}(t)$ of (10) reaches the equilibrium in some finite time, i.e., $\boldsymbol{x}(t) = 0, \forall t \geqslant T(\boldsymbol{x}(0))$, where $T: \mathbb{R}^n \to \mathbb{R}^+$ is called settling-time function.

Definition 2 (*Prescribed-Time Stable* (*PTS*) (*Xu et al., 2021b; Sánchez-Torres et al., 2018*)). The equilibrium of the system (10) is said to be globally *prescribed-time stable* if it is finite-time stable and the settling-time function $T(\boldsymbol{x}(0))$ is bounded by a prescribed time T_c for any $\boldsymbol{x}(0) \in \mathbb{R}^n$, that is, $T(\boldsymbol{x}(0)) \leqslant T_c, \forall \boldsymbol{x}(0) \in \mathbb{R}^n$.

Lemma 2 ((*Anguiano-Gijón et al., 2019; Xu et al., 2021b*)). If there is a Lyapunov function $V: \mathbb{R}^n \to \mathbb{R}_+ \cup \{0\}$ that satisfies

$$\dot{V}(\boldsymbol{x}) \leqslant -\frac{\pi}{vT}\left[V^{1-\frac{v}{2}}(\boldsymbol{x}) + V^{1+\frac{v}{2}}(\boldsymbol{x})\right] \tag{11}$$

where T is a prescribed time and $0 < v < 1$, then the origin of system (10) is globally prescribed-time stable with the least upper-bound of settling time being T.

Lemma 3 ((*Sui et al., 2019; Zou and Fan, 2020*)). Let $x_i \in \mathbb{R}, i = 1, \ldots, n$. Then

$$\left(\sum_{i=1}^{n}|x_i|\right)^{\alpha} \leqslant \sum_{i=1}^{n}|x_i|^{\alpha} \leqslant n^{1-\alpha}\left(\sum_{i=1}^{n}|x_i|\right)^{\alpha}, \text{ if } \alpha \in (0,1], \tag{12}$$

and

$$\left(\sum_{i=1}^{n}|x_i|\right)^{\alpha} \geqslant \sum_{i=1}^{n}|x_i|^{\alpha} \geqslant n^{1-\alpha}\left(\sum_{i=1}^{n}|x_i|\right)^{\alpha}, \text{ if } \alpha \in (1,\infty). \tag{13}$$

3. Main results

In this section, a prescribed-time sliding-mode is first designed such that the position tracking error $\tilde{\boldsymbol{\rho}}_i$and the velocity tracking error $\dot{\tilde{\boldsymbol{\rho}}}_i$ can converge to the origin in a prescribed time on the sliding-mode. Then, based on the prescribed-time sliding-mode, we propose a distributed prescribed-time formation control law and analyze the prescribed-time stability of the system. The control structure is shown in Fig. 2.

Fig. 3 shows the inter-spacecraft relative sensor network of SFF system. The spacecraft in the formation use the onboard measurement equipments, such as, Lidar and optical image sensors, to measure the relative positions and velocities. Compared with the decentralized spacecraft formation control schemes in (Hu and Shi, 2020; Zhuang et al., 2021b), it is not necessary for each spacecraft to measure the relative position and velocity, w.r.t., the reference spacecraft, i.e., $\boldsymbol{\rho}_i$ and $\dot{\boldsymbol{\rho}}_i$, in the proposed control scheme. Only one or several spacecraft need to measure these.

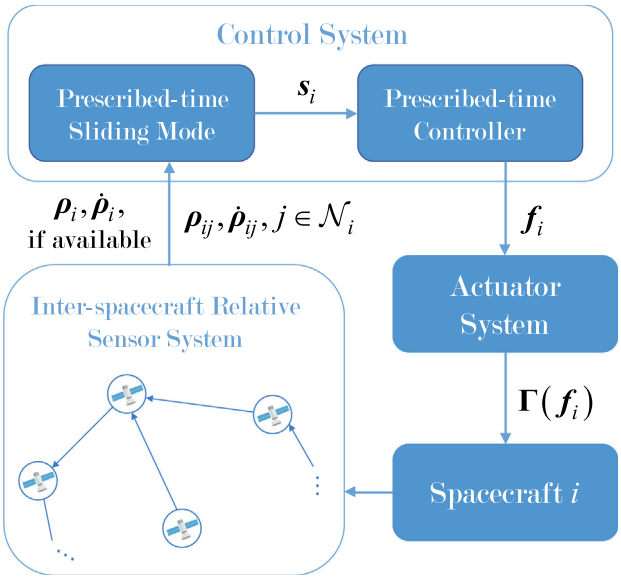

Fig. 2. Control structure of the spacecraft i.

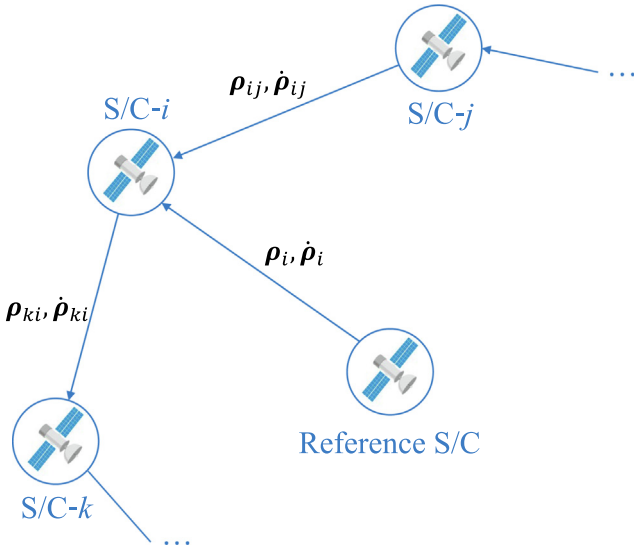

Fig. 3. Inter-spacecraft relative sensor network of the SFF System.

The control problem we aim to solve in this section is stated as follows:

Problem 1. Design control inputs $\boldsymbol{f}_i$ for the input-saturation spacecraft formation system described by (1) using the directed inter-spacecraft sensor network such that ρ_i and $\dot{\rho}_i$ converge to the desired positions $\rho_i^{\star}$ and velocities $\dot{\rho}_i^{\star}$, respectively, in a prescribed time T, that is,

$$\lim_{t\to T}\rho_i = \rho_i^{\star} \text{and} \lim_{t\to T}\dot{\rho}_i = \dot{\rho}_i^{\star},\ i = 1, \ldots, n.$$

To address Problem 1, the following assumptions are needed.

Assumption 1. The second derivatives of the reference relative positions $\ddot{\rho}_i^{\star}$ are bounded by $\|\ddot{\rho}_i^{\star}\| \leqslant c_{d\rho}$, where $c_{d\rho} > 0$ is a known constant.

The spacecraft in the formation need to track the reference relative position $\rho_i^{\star}$ and reference relative velocity $\dot{\rho}_i^{\star}$. If $\ddot{\rho}_i^{\star}$ is very large or even infinity, it is hard to design a bounded control input to track the reference relative velocity $\dot{\rho}_i^{\star}$. Thus, Assumption 1 is reasonable and necessary.

Assumption 2. The disturbances $\boldsymbol{d}_i$ are bounded by $\|\boldsymbol{d}_i\| \leqslant c_d$, where $c_d > 0$ is a known constant.

In practice, the spacecraft in Earth orbit suffers from many types of disturbances, such as, atmospheric drag, third body interaction and the non-spherical shape of the earth perturbations. These disturbances are actually bounded.

Assumption 3. The digraph $\bar{G}$ has a directed spanning tree with the reference spacecraft being the root.

In Assumption 3, it is not necessary for all spacecraft to have access to the reference spacecraft. The desired formation can be tracked when one or several spacecraft can measure the relative positions w.r.t., the reference spacecraft. Furthermore, Assumption 3 is used in the Lemma 1. Without this assumption, it is hard to guarantee all spacecraft to track the desired formation just by measuring the relative positions w.r.t., their neighboring spacecraft.

3.1. Prescribed-time sliding-mode design

In this section, we design a prescribed-time sliding-mode and prove that the states on the sliding mode converge to equilibrium point in prescribed time. To facilitate the controller design, we define a composed position tracking error χ_i including the relative position tracking errors with respect to all its neighbors as

$$\begin{aligned}\chi_i &= a_{i0}\tilde{\boldsymbol{\rho}}_i + \sum_{j\in N_i} a_{ij}\left(\boldsymbol{\rho}_{ij} - \boldsymbol{\rho}_{ij}^{\star}\right)\\ &= a_{i0}\tilde{\boldsymbol{\rho}}_i + \sum_{j\in N_i} a_{ij}\left(\tilde{\boldsymbol{\rho}}_i - \tilde{\boldsymbol{\rho}}_j\right).\end{aligned} \tag{14}$$

The composed velocity tracking error $\dot{\chi}_i$ is defined as

$$\begin{aligned}\dot{\chi}_i &= a_{i0}\dot{\tilde{\boldsymbol{\rho}}}_i + \sum_{j\in N_i} a_{ij}\left(\dot{\boldsymbol{\rho}}_{ij} - \dot{\boldsymbol{\rho}}_{ij}^{\star}\right)\\ &= a_{i0}\dot{\tilde{\boldsymbol{\rho}}}_i + \sum_{j\in N_i} a_{ij}\left(\dot{\tilde{\boldsymbol{\rho}}}_i - \dot{\tilde{\boldsymbol{\rho}}}_j\right).\end{aligned} \tag{15}$$

Define

$\chi = \left[\chi_1^T, \ldots, \chi_n^T\right]^T, \dot{\chi} = \left[\dot{\chi}_1^T, \ldots, \dot{\chi}_n^T\right]^T, \tilde{\boldsymbol{\rho}} = \left[\tilde{\boldsymbol{\rho}}_1^T, \ldots, \tilde{\boldsymbol{\rho}}_n^T\right]^T$ and $\dot{\tilde{\boldsymbol{\rho}}} = \left[\dot{\tilde{\boldsymbol{\rho}}}_1^T, \ldots, \dot{\tilde{\boldsymbol{\rho}}}_n^T\right]^T$. Then, we have

$$\chi = (H \otimes \boldsymbol{I}_3)\tilde{\boldsymbol{\rho}} = \bar{H}\tilde{\boldsymbol{\rho}}, \tag{16}$$

and

$$\dot{\chi} = (H \otimes \boldsymbol{I}_3)\dot{\tilde{\boldsymbol{\rho}}} = \bar{H}\dot{\tilde{\boldsymbol{\rho}}}, \tag{17}$$

where $\bar{H} = H \otimes \boldsymbol{I}_3$.

A prescribed-time sliding-mode is designed as follows.

$$\boldsymbol{s}_i = \dot{\chi}_i + k_s\chi_i + \frac{\pi}{2v_sT_s}\left(V_{\chi_i}^{-v_s/2} + V_{\chi_i}^{v_s/2}\right)\chi_i, \tag{18}$$

where $k_s > 0$ and $0 < v_s < 1$ are some constants, $V_{\chi_i} = \chi_i^T\chi_i/2$, and T_s is the prescribed time.

Theorem 1. If the sliding mode $\boldsymbol{s}_i$ satisfies $\|\boldsymbol{s}_i\| \leqslant \Delta$ with Δ being a positive constant, the errors χ_i and $\dot{\chi}_i$ converge to the region

$$\begin{aligned}&\{(\chi_i, \dot{\chi}_i) | \|\chi_i\| \leqslant l_1\Delta, \|\dot{\chi}_i\| \leqslant \Delta\\ &+k_sl_1\Delta + \frac{\pi}{\sqrt{2}v_sT_s}\left(\left(\frac{(l_1\Delta)^2}{2}\right)^{\frac{1-v_s}{2}} + \left(\frac{(l_1\Delta)^2}{2}\right)^{\frac{1+v_s}{2}}\right)\Bigg\}\end{aligned} \tag{19}$$

in the prescribed time T_s, where $l_1 = 1/\sqrt{\varepsilon(2k_s - \varepsilon)}$, and ε is a prescribed positive constant.

Proof. The candidate Lyapunov function is chosen as $V_{\chi_i} = \chi_i^T\chi_i/2$, and its time derivative is

$$\begin{aligned}\dot{V}_{\chi_i} &= \chi_i^T\dot{\chi}_i\\ &= \chi_i^T\left[\boldsymbol{s}_i - k_s\chi_i - \frac{\pi}{2v_sT_s}\left(V_{\chi_i}^{-v_s/2} + V_{\chi_i}^{v_s/2}\right)\chi_i\right]\\ &= \chi_i^T\boldsymbol{s}_i - k_s\chi_i^T\chi_i - \frac{\pi}{v_sT_s}\left(V_{\chi_i}^{1-v_s/2} + V_{\chi_i}^{1+v_s/2}\right).\end{aligned} \tag{20}$$

Note that

$$\begin{aligned}\chi_i^T\boldsymbol{s}_i &\leqslant \frac{\varepsilon}{2}\|\chi_i\|^2 + \frac{1}{2\varepsilon}\|\boldsymbol{s}_i\|^2\\ &\leqslant \frac{\varepsilon}{2}\|\chi_i\|^2 + \frac{\Delta^2}{2\varepsilon},\end{aligned} \tag{21}$$

where $\varepsilon > 0$ is a constant. Then, substituting (21) into (20) yields

$$\begin{aligned}\dot{V}_{\chi_i} &\leqslant -(2k_s - \varepsilon)V_{\chi_i} + \frac{\Delta^2}{2\varepsilon} - \frac{\pi}{v_sT_s}\left(V_{\chi_i}^{1-v_s/2} + V_{\chi_i}^{1+v_s/2}\right)\\ &= -(2k_s - \varepsilon)\left[V_{\chi_i} - \frac{\Delta^2}{2\varepsilon(2k_s-\varepsilon)}\right]\\ &\quad - \frac{\pi}{v_sT_s}\left(V_{\chi_i}^{1-v_s/2} + V_{\chi_i}^{1+v_s/2}\right).\end{aligned} \tag{22}$$

If $\|\chi_i\| \geqslant \Delta/\sqrt{\varepsilon(2k_s - \varepsilon)} = l_1\Delta$, we have

$$\dot{V}_{\chi_i} \leqslant -\frac{\pi}{v_sT_s}\left(V_{\chi_i}^{1-v_s/2} + V_{\chi_i}^{1+v_s/2}\right). \tag{23}$$

According to Lemma 2, it follows that χ_i converges to the region $\|\chi_i\| \leqslant l_1\Delta$in the time T_s. If $\|\chi_i\| \leqslant l_1\Delta$, the conclusion also holds.

When $\|\chi_i\| \leqslant l_1\Delta$, it follows from (18) that

$$\begin{aligned}\|\dot{\chi}_i\| &= \left\|\boldsymbol{s}_i - k_s\chi_i - \frac{\pi}{2v_sT_s}\left(V_{\chi_i}^{-v_s/2} + V_{\chi_i}^{v_s/2}\right)\chi_i\right\|\\ &\leqslant \|\boldsymbol{s}_i\| + k_s\|\chi_i\| + \frac{\pi}{\sqrt{2}v_sT_s}\left(V_{\chi_i}^{(1-v_s)/2} + V_{\chi_i}^{(1+v_s)/2}\right)\\ &\leqslant \Delta + k_sl_1\Delta\\ &\quad + \frac{\pi}{\sqrt{2}v_sT_s}\left(\left(\frac{(l_1\Delta)^2}{2}\right)^{\frac{1-v_s}{2}} + \left(\frac{(l_1\Delta)^2}{2}\right)^{\frac{1+v_s}{2}}\right).\end{aligned} \tag{24}$$

Therefore, the errors χ_i and $\dot{\chi}_i$ converge to the region (19) in the time T_s if $\boldsymbol{s}_i \leqslant \Delta$.

Corollary 1. On the sliding mode $\boldsymbol{s}_i = \boldsymbol{0}$, the errors χ_i and $\dot{\chi}_i$ converge to the origin in the prescribed time T_s.

3.2. Prescribed-time formation controller design

In this section, based on the prescribed-time sliding mode in the last section, we proposed a distributed coordinated control law to guarantee that the state errors $\tilde{\boldsymbol{\rho}}_i$ and $\dot{\tilde{\boldsymbol{\rho}}}_i$ converge to a bounded region in a prescribed time.

From (18), the time derivative of $\boldsymbol{s}_i$ is derived as

$$\dot{\boldsymbol{s}}_i = \ddot{\boldsymbol{\chi}}_i + \boldsymbol{h}_i, \tag{25}$$

$$\begin{aligned}\boldsymbol{h}_i = \; & k_s\dot{\boldsymbol{\chi}}_i + \tfrac{\pi}{2v_sT_s}\left(V_{\boldsymbol{\chi}_i}^{-v_s/2} + V_{\boldsymbol{\chi}_i}^{v_s/2}\right)\dot{\boldsymbol{\chi}}_i \\ & + \tfrac{\pi}{4T_s}\left(V_{\boldsymbol{\chi}_i}^{v_s/2-1} - V_{\boldsymbol{\chi}_i}^{-1-v_s/2}\right)\left(\boldsymbol{\chi}_i^T\dot{\boldsymbol{\chi}}_i\right)\boldsymbol{\chi}_i.\end{aligned} \tag{26}$$

A distributed coordinated control law is proposed as

$$\begin{aligned}\boldsymbol{f}_i \; & = m_i\left(a_{i0} + \sum_{i\in N_i} a_{ij}\right)^{-1}\left(\sum_{i\in N_i}\tfrac{a_{ij}}{m_j}\left(\boldsymbol{f}_j - \boldsymbol{g}_j - \boldsymbol{f}_{aj}\right)\right. \\ & \left. -\boldsymbol{h}_i - k_{c1}\boldsymbol{s}_i - \tfrac{\pi n^{v_c/2}}{2v_cT_c}\left(V_{si}^{-v_c/2} + V_{si}^{v_c/2}\right)\boldsymbol{s}_i + \boldsymbol{f}_{\text{robust},i}\right) \\ & + \boldsymbol{f}_{ai} + \boldsymbol{g}_i,\end{aligned} \tag{27}$$

where $0 < v_c < 1$ and $k_{c1} > 0$ are some constants, $n = |V|$ is the number of spacecraft, $V_{si} = \boldsymbol{s}_i^T\boldsymbol{s}_i/2$, and T_c is the prescribed time. The term $\boldsymbol{f}_{\text{robust},i}$ is used to suppress the external disturbances, which is defined as

$$\boldsymbol{f}_{\text{robust},i} = -k_{c2}\frac{\boldsymbol{s}_i}{\|\boldsymbol{s}_i\| + \delta}, \tag{28}$$

where $k_{c2} > 0$ and $\delta > 0$ are constants. The adaptive law $\boldsymbol{f}_{ai}$ is used to compensate the difference between the command control force $\boldsymbol{f}_i$ and applied control force $\Gamma(\boldsymbol{f}_i)$, which is defined as

$$\dot{\boldsymbol{f}}_{ai} = -k_{a1}\boldsymbol{f}_{ai} - k_{a2}\text{sign}(\boldsymbol{f}_{ai}) + \Delta\boldsymbol{f}_i \tag{29}$$

where k_{a1} and k_{a2} are positive constants, and $\Delta\boldsymbol{f}_i = \Gamma(\boldsymbol{f}_i) - \boldsymbol{f}_i$.

Remark 1. It can be observed from (29) that $\boldsymbol{f}_{ai}$ converges to the solution of the Eq. (29) and the solution will be $\Delta\boldsymbol{f}_i/k_{a1}$ if k_{a2} is chosen as 0. $\boldsymbol{f}_{ai}$ can be used to adjust the difference between the command control force $\boldsymbol{f}_i$ and applied control force $\Gamma(\boldsymbol{f}_i)$and makes the difference not so significant.

Theorem 2. Consider a spacecraft formation system described by (1). If Assumptions 1–3 hold, and the initial states satisfy $\|\rho(0)\| + \|\dot{\rho}(0)\| + \|\tilde{\rho}(0)\| + \|\dot{\tilde{\rho}}(0)\| \leqslant V_M$ with $V_M$being a constant, the errors $\tilde{\boldsymbol{\rho}}$ and $\dot{\tilde{\boldsymbol{\rho}}}$ converge to the following region

$$\begin{cases}\|\tilde{\boldsymbol{\rho}}\| \leqslant & nl_1c_s\|\bar{H}^{-1}\|, \\ \|\dot{\tilde{\boldsymbol{\rho}}}\| \leqslant & n\|\bar{H}^{-1}\|(c_s + k_sl_1c_s \\ & + \tfrac{\pi}{\sqrt{2}v_sT_s}\left(\left(\tfrac{(l_1c_s)^2}{2}\right)^{\frac{1-v_s}{2}} + \left(\tfrac{(l_1c_s)^2}{2}\right)^{\frac{1+v_s}{2}}\right),\end{cases}$$

in the prescribed time $T_s + T_c$ under the control law in (53)–(29), where $c_s = \sqrt{\frac{k_{c2}n\delta}{k_{c1} - \frac{\|\bar{H}\boldsymbol{m}^{-1}\|}{2\epsilon_1}}}$ and ϵ_1 is a user-designed positive constant.

Proof. To facilitate the proof, we introduce the following notations,

$$\begin{aligned}& \boldsymbol{s} = \left[\boldsymbol{s}_1^T, \ldots, \boldsymbol{s}_n^T\right]^T, \boldsymbol{h} = \left[\boldsymbol{h}_1^T, \ldots, \boldsymbol{h}_n^T\right]^T, \\ & \boldsymbol{g} = \left[\boldsymbol{g}_1^T, \ldots, \boldsymbol{g}_n^T\right]^T, \boldsymbol{f} = \left[\boldsymbol{f}_1^T, \ldots, \boldsymbol{f}_n^T\right]^T, \\ & \Delta\boldsymbol{f} = \left[\Delta\boldsymbol{f}_1^T, \ldots, \Delta\boldsymbol{f}_n^T\right]^T, \boldsymbol{d} = \left[\boldsymbol{d}_1^T, \ldots, \boldsymbol{d}_n^T\right]^T, \\ & \boldsymbol{m} = \text{diag}[m_1\boldsymbol{I}_3, \ldots, m_n\boldsymbol{I}_3], \ddot{\rho}^{\star} = \left[\left(\ddot{\rho}_1^{\star}\right)^T, \ldots, \left(\ddot{\rho}_n^{\star}\right)^T\right]^T, \\ & \boldsymbol{f}_a = \left[\boldsymbol{f}_{a,1}^T, \ldots, \boldsymbol{f}_{a,n}^T\right]^T, \boldsymbol{f}_{\text{robust}} = \left[\boldsymbol{f}_{\text{robust},1}^T, \ldots, \boldsymbol{f}_{\text{robust},n}^T\right]^T.\end{aligned} \tag{30}$$

Eq. (53) can be rewritten as

$$\begin{aligned}\boldsymbol{f} \; & = \boldsymbol{m}\left[(A_0 + D)^{-1} \otimes \boldsymbol{I}_3\right][(A \otimes \boldsymbol{I}_3)\boldsymbol{m}^{-1}(\boldsymbol{f} - \boldsymbol{g} - \boldsymbol{f}_a) \\ & -\boldsymbol{h} - k_{c1}\boldsymbol{s} - \tfrac{\pi n^{v_c/2}}{2v_cT_c}\left(\text{diag}\left\{V_{si}^{-v_c/2} + V_{si}^{v_c/2}\right\} \otimes \boldsymbol{I}_3\right)\boldsymbol{s} \\ & + \boldsymbol{f}_{\text{robust}}] + \boldsymbol{g} + \boldsymbol{f}_a,\end{aligned} \tag{31}$$

where $D = L + A$ is the in-degree matrix of the sensing graph. It follows from (31) that

$$\begin{aligned}\boldsymbol{f} \; & = \left[\boldsymbol{I}_{3n} - \boldsymbol{m}\left(\left((A_0 + D)^{-1}A\right) \otimes \boldsymbol{I}_3\right)\boldsymbol{m}^{-1}\right]^{-1} \\ & \times \boldsymbol{m}\left((A_0 + D)^{-1} \otimes \boldsymbol{I}_3\right)[-\boldsymbol{h} - k_{c1}\boldsymbol{s} \\ & - \tfrac{\pi n^{v_c/2}}{2v_cT_c}\left(\text{diag}\left\{V_{si}^{-v_c/2} + V_{si}^{v_c/2}\right\} \otimes \boldsymbol{I}_3\right)\boldsymbol{s} + \boldsymbol{f}_{\text{robust}}] \\ & + \boldsymbol{g} + \boldsymbol{f}_a \\ & = \boldsymbol{m}\bar{H}^{-1}\left[-\tfrac{\pi n^{v_c/2}}{2v_cT_c}\left(\text{diag}\left\{V_{si}^{-v_c/2} + V_{si}^{v_c/2}\right\} \otimes \boldsymbol{I}_3\right)\boldsymbol{s}\right. \\ & \left. -\boldsymbol{h} - k_{c1}\boldsymbol{s} + \boldsymbol{f}_{\text{robust}}\right] + \boldsymbol{g} + \boldsymbol{f}_a,\end{aligned} \tag{32}$$

where the following equality is applied.

$$\begin{aligned}& \boldsymbol{I}_{3n} - \boldsymbol{m}\left(\left((A_0 + D)^{-1}A\right) \otimes \boldsymbol{I}_3\right)\boldsymbol{m}^{-1} \\ & = \boldsymbol{m}\left((A_0 + D)^{-1} \otimes \boldsymbol{I}_3\right)[(A_0 + D) \otimes \boldsymbol{I}_3 - A \otimes \boldsymbol{I}_3]\boldsymbol{m}^{-1} \\ & = \boldsymbol{m}\left((A_0 + D)^{-1} \otimes \boldsymbol{I}_3\right)\bar{H}\boldsymbol{m}^{-1}.\end{aligned} \tag{33}$$

Substituting (32) into the time derivative of $\boldsymbol{s}$ yields

$$\begin{aligned}\dot{\boldsymbol{s}} \; & = \bar{H}\ddot{\tilde{\boldsymbol{\rho}}} + \boldsymbol{h} \\ & = \bar{H}\boldsymbol{m}^{-1}(-\boldsymbol{g} + \boldsymbol{f} + \Delta\boldsymbol{f} + \boldsymbol{d}) - \bar{H}\ddot{\rho}^{\star} + \boldsymbol{h} \\ & = -k_{c1}\boldsymbol{s} - \tfrac{\pi n^{v_c/2}}{2v_cT_c}\text{diag}\left(\left\{V_{si}^{-v_c/2} + V_{si}^{v_c/2}\right\} \otimes \boldsymbol{I}_3\right)\boldsymbol{s} \\ & + \boldsymbol{f}_{\text{robust}} + \bar{H}\boldsymbol{m}^{-1}(\boldsymbol{f}_a + \Delta\boldsymbol{f} + \boldsymbol{d}) - \bar{H}\ddot{\rho}^{\star}.\end{aligned} \tag{34}$$

The proof contains two parts: In the part I, it is proved that $\boldsymbol{f}_a$ is bounded. In the part II, it is proved that $\boldsymbol{s}$ converges to the region D_s within the time $T_s + T_c$.

Part I: The candidate Lyapunov function is chosen as

$$V_1 = \frac{1}{2}\boldsymbol{s}^T\boldsymbol{s} + \frac{1}{2}\boldsymbol{f}_a^T\boldsymbol{f}_a. \tag{35}$$

The time derivative of V_1 is

$$\begin{aligned}
\dot{V}_1 = \;& \boldsymbol{s}^T\dot{\boldsymbol{s}} + \boldsymbol{f}_a^T\dot{\boldsymbol{f}}_a \\
= \;& -k_{c1}\|\boldsymbol{s}\|^2 - \tfrac{\pi n^{v_c/2}}{v_c T_c}\sum_{i=1}^{n}\left(V_{si}^{1-v_c/2} + V_{si}^{1+v_c/2}\right) \\
& + \boldsymbol{s}^T\boldsymbol{f}_{\text{robust}} + \boldsymbol{s}^T\bar{H}\boldsymbol{m}^{-1}(\boldsymbol{f}_a + \Delta\boldsymbol{f} + \boldsymbol{d}) \\
& - \boldsymbol{s}^T\bar{H}\ddot{\rho}^{\star} - k_{a1}\boldsymbol{f}_a^T\boldsymbol{f}_a - k_{a2}\|\boldsymbol{f}_a\| + \boldsymbol{f}_a^T\Delta\boldsymbol{f} \\
\leqslant \;& -\left(k_{c1} - \tfrac{\|\bar{H}\boldsymbol{m}^{-1}\|}{2\epsilon_1}\right)\|\boldsymbol{s}\|^2 \\
& - \tfrac{\pi n^{v_c/2}}{v_c T_c}\sum_{i=1}^{n}\left(V_{si}^{1-v_c/2} + V_{si}^{1+v_c/2}\right) + \boldsymbol{s}^T\boldsymbol{f}_{\text{robust}} \\
& + \|\boldsymbol{s}\| \times \|\bar{H}\|(\|\boldsymbol{m}^{-1}\| \times \|\Delta\boldsymbol{f} + \boldsymbol{d}\| + \|\ddot{\rho}^{\star}\|) \\
& - \left(k_{a1} - \tfrac{\epsilon_1\|\bar{H}\boldsymbol{m}^{-1}\|}{2}\right)\|\boldsymbol{f}_a\|^2 - k_{a2}\|\boldsymbol{f}_a\| + \boldsymbol{f}_a^T\Delta\boldsymbol{f},
\end{aligned} \tag{36}$$

where the following inequality is applied.

$$\begin{aligned}
\boldsymbol{s}^T\bar{H}\boldsymbol{m}^{-1}\boldsymbol{f}_a \leqslant \;& \|\boldsymbol{s}\| \times \|\bar{H}\boldsymbol{m}^{-1}\| \times \|\boldsymbol{f}_a\| \\
\leqslant \;& \tfrac{\|\bar{H}\boldsymbol{m}^{-1}\|}{2\epsilon_1}\|\boldsymbol{s}\|^2 + \tfrac{\epsilon_1\|\bar{H}\boldsymbol{m}^{-1}\|}{2}\|\boldsymbol{f}_a\|^2
\end{aligned} \tag{37}$$

where ϵ_1 is a positive constant.

Note that $\boldsymbol{s}^T\boldsymbol{f}_{\text{robust}} = \left[\boldsymbol{f}_{\text{robust},1}^T\boldsymbol{s}_1, \ldots, \boldsymbol{f}_{\text{robust},n}^T\boldsymbol{s}_n\right]^T$, and

$$\boldsymbol{f}_{\text{robust},i}^T\boldsymbol{s}_i = -k_{c2}\frac{\|\boldsymbol{s}_i\|^2}{\|\boldsymbol{s}_i\| + \delta} \leqslant -k_{c2}\|\boldsymbol{s}_i\| + k_{c2}\delta. \tag{38}$$

According to Lemma 3, we have

$$\begin{aligned}
\boldsymbol{s}^T\boldsymbol{f}_{\text{robust}} &= \sum_{i=1}^{n}\boldsymbol{f}_{\text{robust},i}^T\boldsymbol{s}_i \\
&\leqslant -k_{c2}\sum_{i=1}^{n}\|\boldsymbol{s}_i\| + k_{c2}n\delta \\
&\leqslant -k_{c2}\|\boldsymbol{s}\| + k_{c2}n\delta.
\end{aligned} \tag{39}$$

In this proof, we use the forward-invariant set theory (Krastanov, 1995) to analyze the system stability. First, we need to construct the following set.

$$\Pi = \left\{(\rho, \dot{\rho}, \tilde{\rho}, \dot{\tilde{\rho}}) \,|\, \|\rho\| + \|\dot{\rho}\| + \|\tilde{\rho}\| + \|\dot{\tilde{\rho}}\| \leqslant V_M\right\}. \tag{40}$$

In the set Π, the control force $\boldsymbol{f}$ is bounded. This implies that $\|\Delta\boldsymbol{f}\| \leqslant c_{\Delta f}$, where $c_{\Delta f} > 0$ is a constant. According to Assumptions 1 and 2, the reference states $\ddot{\rho}_i^{\star}$ and external disturbance $\boldsymbol{d}_i$ are bounded by $\|\ddot{\rho}_i^{\star}\| \leqslant c_{d\rho}$ and $\|\boldsymbol{d}_i\| \leqslant \boldsymbol{c}_{\boldsymbol{d}}$, respectively. According to Lemma 3, it follows that $\|\ddot{\rho}^{\star}\| \leqslant nc_{d\rho}$ and $\|\boldsymbol{d}\| \leqslant \boldsymbol{nc}_{\boldsymbol{d}}$. From (36) and (39), we have

$$\begin{aligned}
\dot{V}_1 \leqslant \;& -\left(k_{c1} - \tfrac{\|\bar{H}\boldsymbol{m}^{-1}\|}{2\epsilon_1}\right)\|\boldsymbol{s}\|^2 \\
& - \tfrac{\pi n^{v_c/2}}{v_c T_c}\sum_{i=1}^{n}\left(V_{si}^{1-v_c/2} + V_{si}^{1+v_c/2}\right) + k_{c2}n\delta \\
& - \left[k_{c2} - \|\bar{H}\|\left(\|\boldsymbol{m}^{-1}\|(c_{\Delta f} + nc^{\star}) + nc_{d\rho}\right)\right]\|\boldsymbol{s}\| \\
& - \left(k_{a1} - \tfrac{\epsilon_1\|\bar{H}\boldsymbol{m}^{-1}\|}{2}\right)\|\boldsymbol{f}_a\|^2 - (k_{a2} - c_{\Delta f})\|\boldsymbol{f}_a\| \\
\leqslant \;& -\left(k_{c1} - \tfrac{\|\bar{H}\boldsymbol{m}^{-1}\|}{2\epsilon_1}\right)\|\boldsymbol{s}\|^2 \\
& - \tfrac{\pi n^{v_c/2}}{v_c T_c}\sum_{i=1}^{n}\left(V_{si}^{1-v_c/2} + V_{si}^{1+v_c/2}\right) + k_{c2}n\delta \\
& - \left(k_{a1} - \tfrac{\epsilon_1\|\bar{H}\boldsymbol{m}^{-1}\|}{2}\right)\|\boldsymbol{f}_a\|^2,
\end{aligned} \tag{41}$$

where $k_{c1} - \frac{\|\bar{H}\boldsymbol{m}^{-1}\|}{2\epsilon_1} > 0, k_{c2} - \|\bar{H}\|\left(\|\boldsymbol{m}^{-1}\|(c_{\Delta f} + nc_d) + nc_{d\rho}\right) > 0$, $k_{a1} - \frac{\epsilon_1\|\bar{H}\boldsymbol{m}^{-1}\|}{2} > 0$ and $k_{a2} - c_{\Delta f} > 0$.

From (41), we have

$$\begin{aligned}
\dot{V}_1 \leqslant \;& -\left(k_{c1} - \tfrac{\|\bar{H}\boldsymbol{m}^{-1}\|}{2\epsilon_1}\right)\left(\|\boldsymbol{s}\|^2 - \tfrac{k_{c2}n\delta}{k_{c1} - \frac{\|\bar{H}\boldsymbol{m}^{-1}\|}{2\epsilon_1}}\right) \\
& - \tfrac{\pi n^{v_c/2}}{v_c T_c}\sum_{i=1}^{n}\left(V_{si}^{1-v_c/2} + V_{si}^{1+v_c/2}\right) \\
& - \left(k_{a1} - \tfrac{\epsilon_1\|\bar{H}\boldsymbol{m}^{-1}\|}{2}\right)\|\boldsymbol{f}_a\|^2,
\end{aligned} \tag{42}$$

or

$$\begin{aligned}
\dot{V}_1 \leqslant \;& -\left(k_{c1} - \tfrac{\|\bar{H}\boldsymbol{m}^{-1}\|}{2\epsilon_1}\right)\|\boldsymbol{s}\|^2 \\
& - \tfrac{\pi n^{v_c/2}}{v_c T_c}\sum_{i=1}^{n}\left(V_{si}^{1-v_c/2} + V_{si}^{1+v_c/2}\right) \\
& - \left(k_{a1} - \tfrac{\epsilon_1\|\bar{H}\boldsymbol{m}^{-1}\|}{2}\right)\left(\|\boldsymbol{f}_a\|^2 - \tfrac{k_{c2}n\delta}{k_{a1} - \frac{\epsilon_1\|\bar{H}\boldsymbol{m}^{-1}\|}{2}}\right).
\end{aligned} \tag{43}$$

If $\|\boldsymbol{s}\| \geqslant \sqrt{\frac{k_{c2}n\delta}{k_{c1} - \frac{\|\bar{H}\boldsymbol{m}^{-1}\|}{2\epsilon_1}}}$ or $\|\boldsymbol{f}_a\| \geqslant \sqrt{-\frac{k_{c2}n\delta}{k_{a1} - \frac{\epsilon_1\|\bar{H}\boldsymbol{m}^{-1}\|}{2}}} \triangleq c_{f_a}$, it follows from (42) and (43) that

$$\dot{V}_1 \leqslant -\frac{\pi n^{v_c/2}}{v_c T_c}\sum_{i=1}^{n}\left(V_{si}^{1-v_c/2} + V_{si}^{1+v_c/2}\right). \tag{44}$$

According to Lemma 2, it follows from (44) that $\boldsymbol{s}$ and $\boldsymbol{f}_a$ converge to the following region.

$$\left\{(\boldsymbol{s}, \boldsymbol{f}_a) \,\middle|\, \|\boldsymbol{s}\| \leqslant \sqrt{\frac{k_{c2}n\delta}{k_{c1} - \frac{\|\bar{H}\boldsymbol{m}^{-1}\|}{2\epsilon_1}}}, \|\boldsymbol{f}_a\| \leqslant c_{f_a}\right\}. \tag{45}$$

According to the forward-invariant set theory (Krastanov, 1995), $(\rho, \dot{\rho}, \tilde{\rho}, \dot{\tilde{\rho}}) \in \Pi$ always holds if $(\rho(0), \dot{\rho}(0), \tilde{\rho}(0), \dot{\tilde{\rho}}(0)) \in \Pi$. Thus, $\boldsymbol{f}_a$ is bounded by $\|\boldsymbol{f}_a\| \leqslant c_{f_a}$ if $(\rho(0), \dot{\rho}(0), \tilde{\rho}(0), \dot{\tilde{\rho}}(0)) \in \Pi$.

Part II: The candidate Lyapunov function is chosen as

$$V_s = \frac{1}{2}\boldsymbol{s}^T\boldsymbol{s}. \tag{46}$$

The time derivative of V_s is

$$\begin{aligned}\dot{V}_s &= -k_{c1}\|\boldsymbol{s}\|^2 - \frac{\pi n^{v_c/2}}{v_c T_c}\sum_{i=1}^{n}\left(V_{si}^{1-v_c/2} + V_{si}^{1+v_c/2}\right)\\ &\quad + \boldsymbol{s}^T\boldsymbol{f}_{\text{robust}} + \boldsymbol{s}^T\bar{H}\boldsymbol{m}^{-1}(\Delta\boldsymbol{f} + \boldsymbol{d} + \boldsymbol{f}_a) - \boldsymbol{s}^T\bar{H}\ddot{\rho}^{\star}\\ &\leqslant -\left(k_{c1} - \frac{\|\bar{H}\boldsymbol{m}^{-1}\|}{2\epsilon_1}\right)\|\boldsymbol{s}\|^2\\ &\quad - \frac{\pi n^{v_c/2}}{v_c T_c}\sum_{i=1}^{n}\left(V_{si}^{1-v_c/2} + V_{si}^{1+v_c/2}\right) + k_{c2}n\delta\\ &\quad - \left[k_{c2} - c_{f_a} - \|\bar{H}\|\left(\|\boldsymbol{m}^{-1}\|(c_{\Delta f} + nc_d) + nc_{d\rho}\right)\right]\|\boldsymbol{s}\|\\ &\leqslant -\left(k_{c1} - \frac{\|\bar{H}\boldsymbol{m}^{-1}\|}{2\epsilon_1}\right)\left(\|\boldsymbol{s}\|^2 - \frac{k_{c2}n\delta}{k_{c1} - \frac{\|\bar{H}\boldsymbol{m}^{-1}\|}{2\epsilon_1}}\right)\\ &\quad - \frac{\pi n^{v_c/2}}{v_c T_c}\sum_{i=1}^{n}\left(V_{si}^{1-v_c/2} + V_{si}^{1+v_c/2}\right),\end{aligned} \tag{47}$$

where $k_{c2} - c_{f_a} - \|\bar{H}\|\left(\|\boldsymbol{m}^{-1}\|(c_{\Delta f} + nc_d) + nc_{d\rho}\right) > 0$.

If $\|\boldsymbol{s}\| \geqslant \sqrt{\frac{k_{c2}n\delta}{k_{c1} - \frac{\|\bar{H}\boldsymbol{m}^{-1}\|}{2\epsilon_1}}} = c_s$, then (47) becomes

$$\begin{aligned}\dot{V}_s &\leqslant -\frac{\pi n^{v_c/2}}{v_c T_c}\sum_{i=1}^{n}\left(V_{si}^{1-v_c/2} + V_{si}^{1+v_c/2}\right)\\ &\leqslant -\frac{\pi n^{v_c/2}}{v_c T_c}\left(V_s^{1-v_c/2} + n^{-v_c/2}V_s^{1+v_c/2}\right)\\ &\leqslant -\frac{\pi}{v_c T_c}\left(V_s^{1-v_c/2} + V_s^{1+v_c/2}\right),\end{aligned} \tag{48}$$

where Lemma 3 is applied. According to Lemma 2, the sliding mode $\boldsymbol{s}$ converges to the region $\{\boldsymbol{s}|\|\boldsymbol{s}\| \leqslant c_s\}$ in the

Table 1
Initial conditions of four spacecraft.

S/C	x_0(m)	y_0 (m)	z_0 (m)	$\dot{x}_0$ (m/s)	$\dot{y}_0$ (m/s)	$\dot{z}_0$(m/s)
No. 1	117.58	-868.74	69.53	−0.479	-0.26	0
No. 2	-431.76	253.62	−213.99	0.140	0.95	0
No. 3	−19.94	899.12	-69.53	0.496	0.04	0
No. 4	437.34	211.97	213.99	0.117	-0.97	0

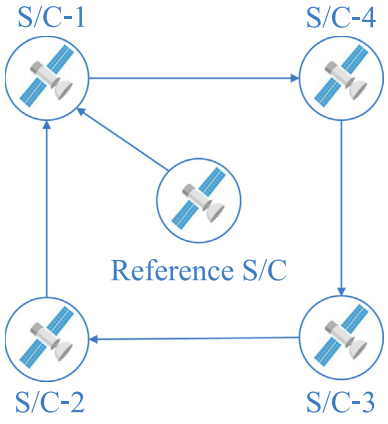

Fig. 4. The sensor topology of SFF.

Table 2
Simulation parameters.

Names	Values
Parameters of the sliding mode $\boldsymbol{s}_i$	$k_s = 0.3, v_s = 0.1, T_s = 20$ sec.
Parameters of the controller $\boldsymbol{f}_i$	$k_{c1} = 0.01, k_{c2} = 0.0002$ $v_c = 0.5, T_c = 500$ sec, $\delta = 0.0001$.
Parameters of the adaptive law $\boldsymbol{f}_{ai}$	$k_{a1} = 1, k_{a2} = 0.001, v_a = 0.1, T_a = 10$ sec.
Maximum allowable force f_M	$f_M = 5$ N.
Mass of spacecraft m_i	$m_i = 100$ kg, $i = 1, 2, 3, 4$.
Weighted adjacency matrix A and A_0	$A = 0.5[0\ 1\ 0\ 0;\ 0\ 0\ 1\ 0;\ 0\ 0\ 0\ 1;\ 1\ 0\ 0\ 0]$ $A_0 = [1\ 0\ 0\ 0;\ 0\ 0\ 0\ 0;\ 0\ 0\ 0\ 0;\ 0\ 0\ 0\ 0]$

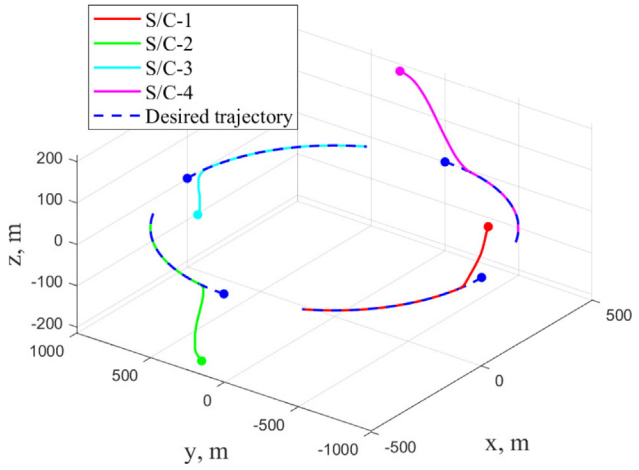

(a) in three-dimensional space.

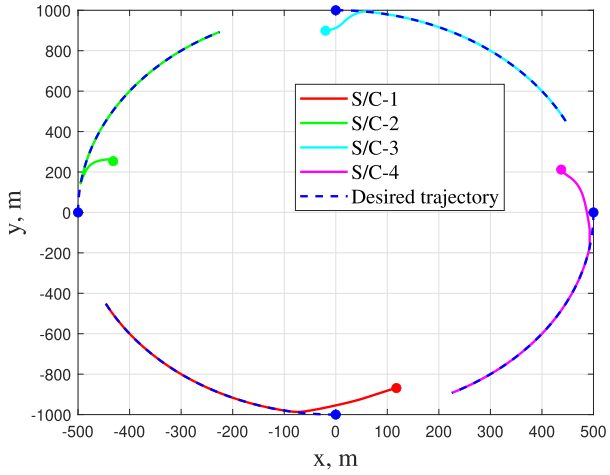

(b) on the x-y plane.

Fig. 5. Tracking trajectories of four spacecraft in three-dimensional space and on the x-y plane. The initial positions are marked with dots. The desired trajectories are marked in blue dashed lines.

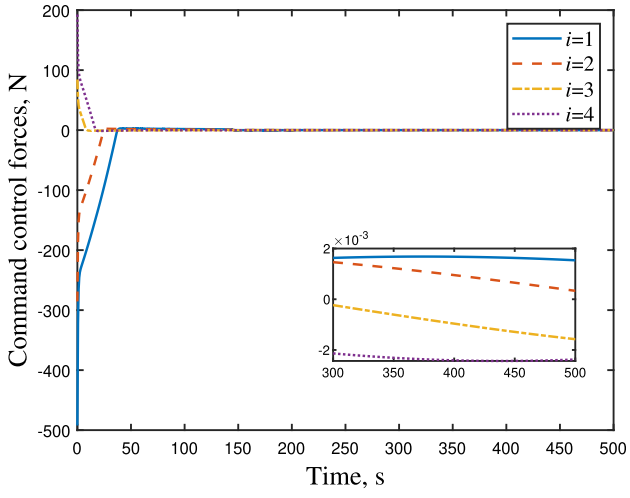

(a) Command control forces $f_{i,x}$.

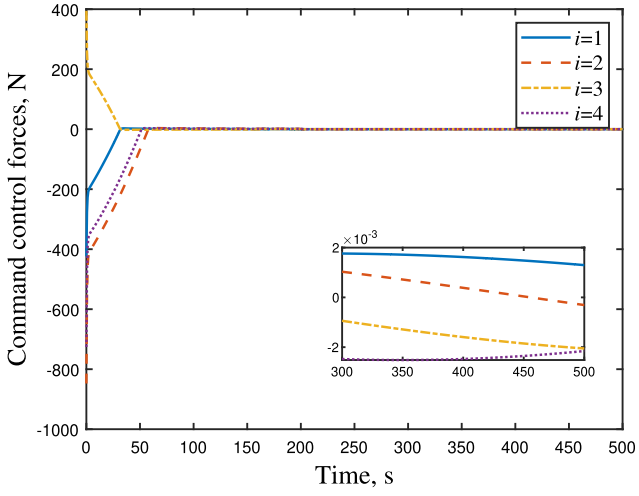

(b) Command control forces $f_{i,y}$.

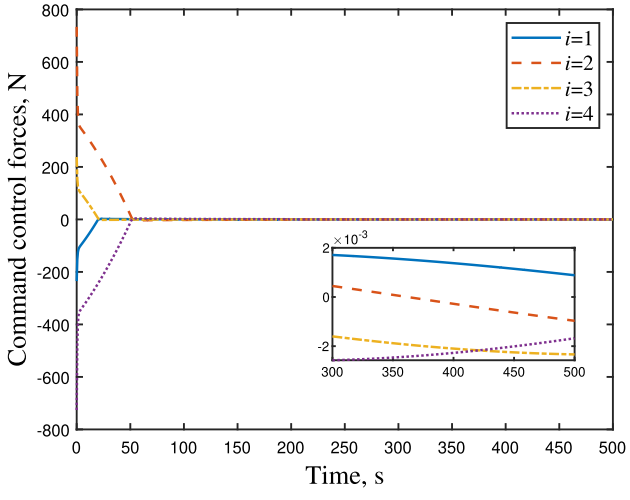

(c) Command control forces $f_{i,z}$.

Fig. 6. Command control forces $\boldsymbol{f}_i = \left[f_{i,x}, f_{i,y}, f_{i,z}\right]^T$ (53).

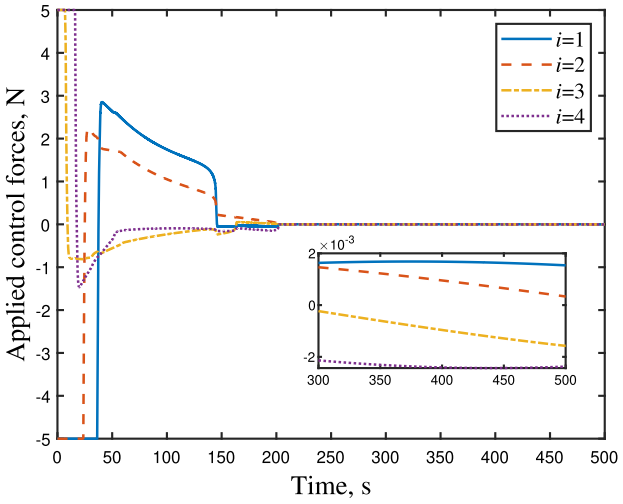

(a) Applied control forces $\Gamma\left(f_{i,x}\right)$.

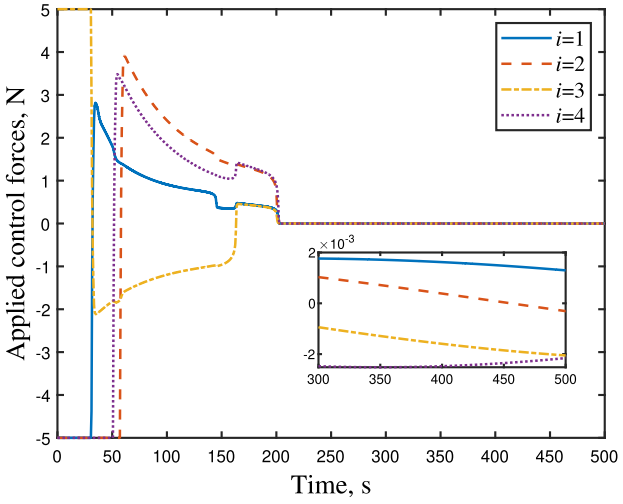

(b) Applied control forces $\Gamma\left(f_{i,y}\right)$.

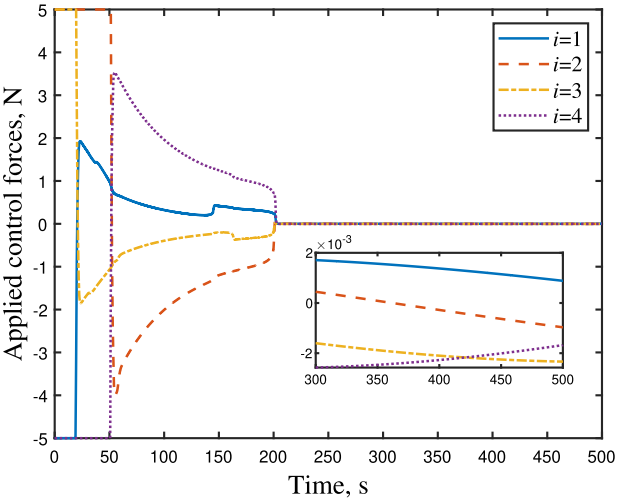

(c) Applied control forces $\Gamma\left(f_{i,z}\right)$.

Fig. 7. Applied control forces $\Gamma(\boldsymbol{f}_i)$.

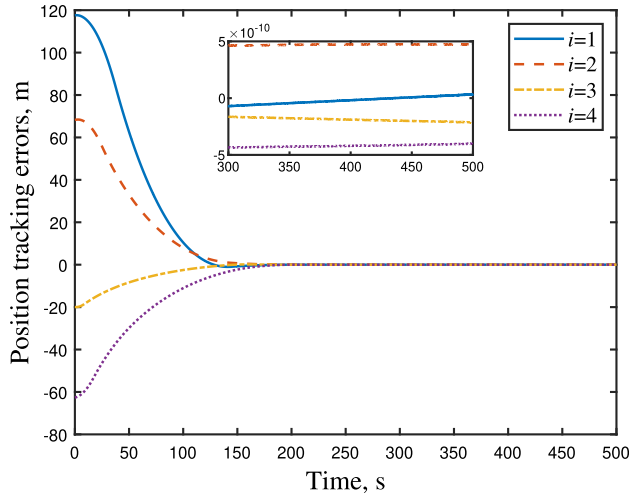

(a) Position tracking errors $\tilde{x}_i$.

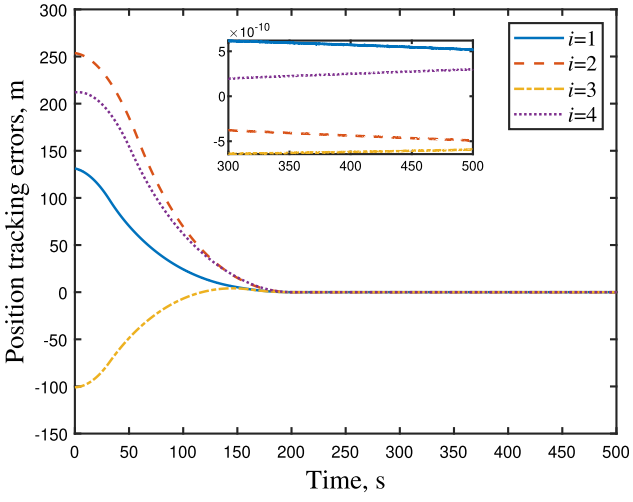

(b) Position tracking errors $\tilde{y}_i$.

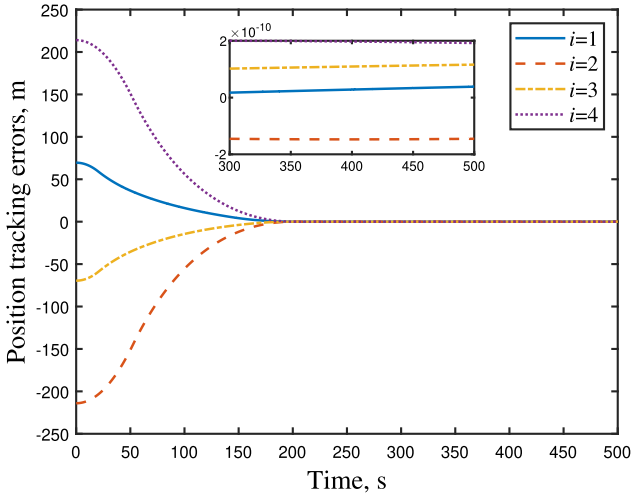

(c) Position tracking errors $\tilde{z}_i$.

Fig. 8. Position tracking errors $\tilde{\boldsymbol{\rho}}_i = [\tilde{x}_i, \tilde{y}_i, \tilde{z}_i]^T$ under the controller (53).

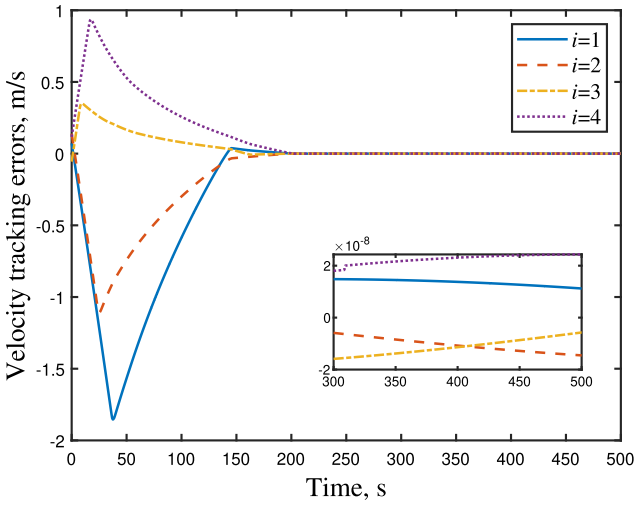

(a) Velocity tracking errors $\dot{\tilde{x}}_i$.

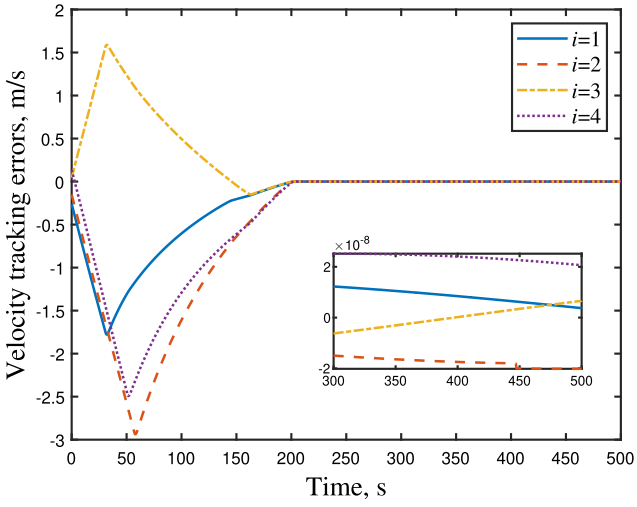

(b) Velocity tracking errors $\dot{\tilde{y}}_i$.

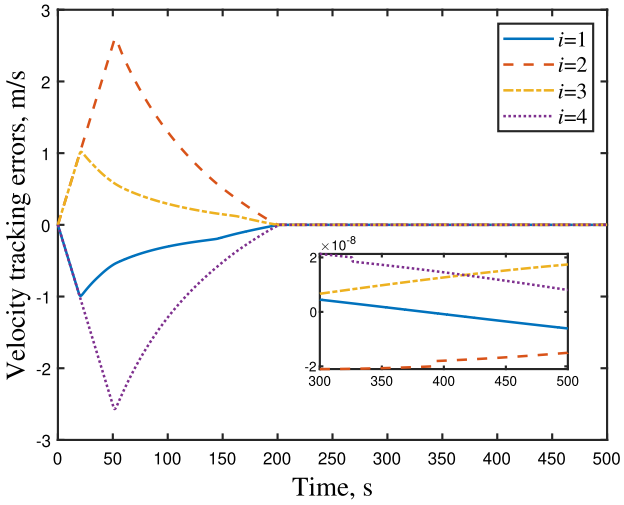

(c) Velocity tracking errors $\dot{\tilde{z}}_i$.

Fig. 9. Velocity tracking errors $\dot{\tilde{\boldsymbol{\rho}}}_i = \left[\dot{\tilde{x}}_i, \dot{\tilde{y}}_i, \dot{\tilde{z}}_i\right]^T$ under the controller (53).

prescribed time T_c. Invoking Theorem 1, it follows that the state errors χ_i and $\dot{\chi}_i$ converge to the following region

$$\{(\chi_i,\dot{\chi}_i)|\|\chi_i\|\leqslant l_1\Delta,\|\dot{\chi}_i\|\leqslant\Delta +k_s l_1\Delta+\frac{\pi}{\sqrt{2}v_sT_s}\left(\left(\frac{(l_1\Delta)^2}{2}\right)^{\frac{1-v_s}{2}}+\left(\frac{(l_1\Delta)^2}{2}\right)^{\frac{1+v_s}{2}}\right)\}$$

in the prescribed time T_s if $\|\boldsymbol{s}\|\leqslant c_s$. According to Lemma 1, the matrix $\bar{H}$ is invertible when Assumption 3 holds. Since $\chi=\bar{H}\tilde{\boldsymbol{\rho}},\dot{\chi}=\bar{H}\dot{\tilde{\boldsymbol{\rho}}}$, and the matrix $\bar{H}$ is invertible, we have

$$\begin{cases}\|\tilde{\boldsymbol{\rho}}\|\leqslant & nl_1c_s\|\bar{H}^{-1}\|,\\ \|\dot{\tilde{\boldsymbol{\rho}}}\|\leqslant & n\|\bar{H}^{-1}\|(c_s+k_sl_1c_s\\ & +\frac{\pi}{\sqrt{2}v_sT_s}\left(\left(\frac{(l_1c_s)^2}{2}\right)^{\frac{1-v_s}{2}}+\left(\frac{(l_1c_s)^2}{2}\right)^{\frac{1+v_s}{2}}\right),\end{cases}\tag{49}$$

Therefore, the errors $\tilde{\boldsymbol{\rho}}_i$ and $\dot{\tilde{\boldsymbol{\rho}}}_i$ converge to a bounded region in the prescribed time T_s+T_c under the control law in (53)–(29).

Table 3
Total velocity change ΔV calculations.

	S/C-1	S/C-2	S/C-3	S/C-4	Total
ΔV (m/s)	7.210	10.600	5.553	9.604	32.967

4. Simulation

In this section, we carry out a simulation example to illustrate the effectiveness of the proposed prescribed-time controller. In the simulation example, we consider a four-spacecraft formation, whose initial conditions in LVLH frame and sensor topology are given in Table 1 and Fig. 4, respectively. The reference spacecraft is a visual

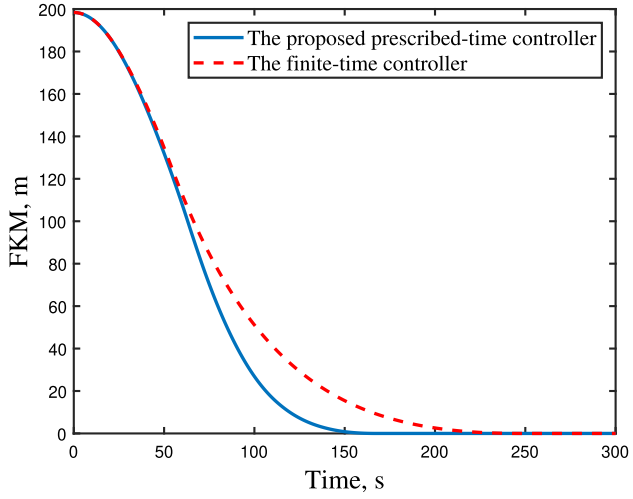

(a) FKM

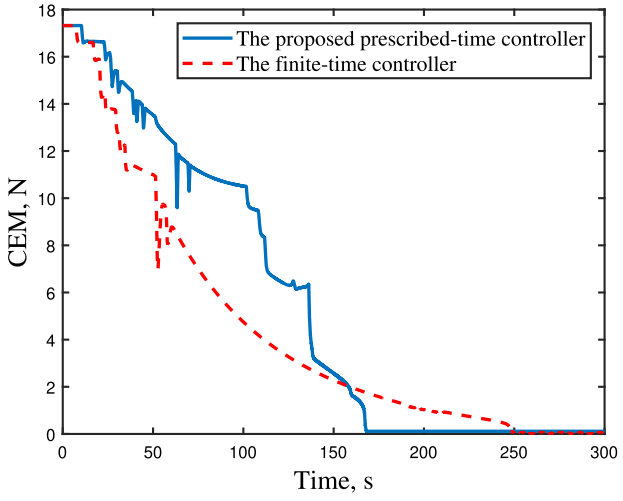

(b) CEM

Fig. 10. Performance comparison between the proposed prescribed-time controller and a finite-time coordinated tracking controller.

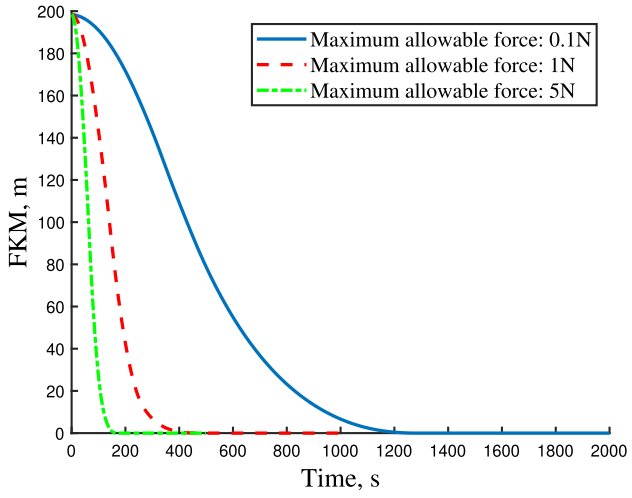

(a) FKM

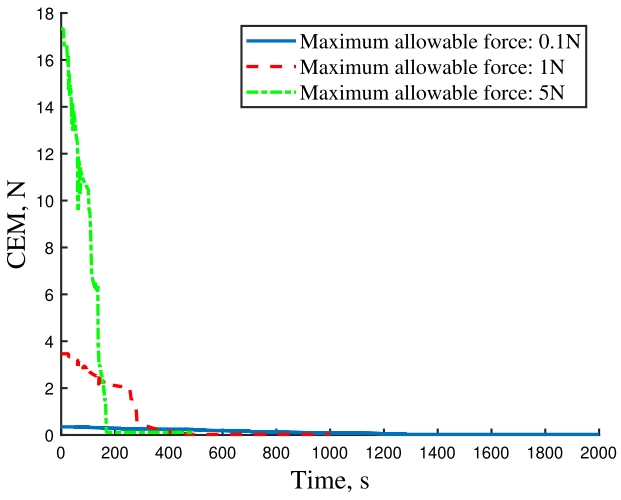

(b) CEM

Fig. 11. Performance comparison under proposed controller with 0.1 N, 1 N and 5 N maximum allowable force.

spacecraft. Its orbit is an elliptical orbit with $a_r = 6892.38$ km, $e_r = 0.01, i_r = 45$ deg, $\omega_r = 30$ deg, $\Omega_r = 145$ deg, and $\theta_r = 0$ deg.

The desired spacecraft formation is chosen as a ring formation, whose initial values $\boldsymbol{\rho}_i^{\star}(0) = \left[x_i^{\star}(0), y_i^{\star}(0), z_i^{\star}(0)\right]^T$ (the unit is m) and $\dot{\boldsymbol{\rho}}_i^{\star}(0) = \left[\dot{x}_i^{\star}(0), \dot{y}_i^{\star}(0), \dot{z}_i^{\star}(0)\right]^T$ (the unit is m/s) are

$$\begin{aligned} &x_i^{\star}(0) = 500\cos\tfrac{\pi i}{2}, \dot{x}_i^{\star}(0) = -500 n_r \sin\tfrac{\pi i}{2}, \\ &y_i^{\star}(0) = 2\dot{x}_i^{\star}(0)/n_r, \dot{y}_i^{\star}(0) = -2n_r x_i^{\star}(0), \\ &z_i^{\star}(0) = 0, \dot{z}_i^{\star}(0) = 0, i = 1,2,3,4. \end{aligned} \tag{50}$$

The desired trajectories $\boldsymbol{\rho}_i^{\star} = \left[x_i^{\star}, y_i^{\star}, z_i^{\star}\right]^T, i = 1,2,3,4$, are chosen as the solution of the linearized relative motion dynamics in (Pini Gurfil, 2007), which is given by

$$\begin{aligned} x_i^{\star}(t) = &-\left(3x_i^{\star}(0) + \tfrac{2}{n_r}\dot{y}_i^{\star}(0)\right)\cos(n_r t) + \tfrac{\dot{x}_i^{\star}(0)}{n_r}\sin(n_r t) \\ &+ \tfrac{2}{n_r}\dot{y}_i^{\star}(0) + 4x_i^{\star}(0), \\ y_i^{\star}(t) = &\ 6(\sin(n_r t) - n_r t)x_i^{\star}(0) + y_i^{\star}(0) \\ &+ \tfrac{2}{n_r}(\cos(n_r t) - 1)\dot{x}_i^{\star}(0) + (4\sin(n_r t) - 3n_r t)\tfrac{\dot{y}_i^{\star}(0)}{n_r}, \\ z_i^{\star}(t) = &\ z_i^{\star}(0)\cos(n_r t) + \tfrac{\dot{z}_i^{\star}(0)}{n_r}\sin(n_r t). \end{aligned} \tag{51}$$

The corresponding desired trajectories $\boldsymbol{\rho}_{ij}^{\star}$ can be calculated by $\boldsymbol{\rho}_{ij}^{\star} = \boldsymbol{\rho}_i^{\star} - \boldsymbol{\rho}_j^{\star}, (i,j) \in E$.

4.1. Simulation of the proposed prescribed-time Coordinated controller

In this simulation, the simulation parameters are given in Table 2. The J_2 perturbations and atmospheric drag perturbations are both considered. The shape of each spacecraft is different, which yields that there is a little difference on the atmospheric drag perturbations of each spacecraft. Thus, the atmospheric drag perturbations of the spacecraft 1 to 4 are selected as 0.9×10^{-8} N, 1×10^{-8} N, 1.1×10^{-8} N, and 1.2×10^{-8} N, respectively. Fig. 5 shows the tracking trajectories of four spacecraft in three-dimensional space and on the x-y plane under the controller (53). The initial positions of the spacecraft and desired trajectories are marked with dots. Fig. 6 and 7 show the command control forces $\boldsymbol{f}_i$ and the applied control forces $\Gamma(\boldsymbol{f}_i)$, respectively. The maximum allowable force f_M is chosen as 5 N. Thus, although the command control forces $\boldsymbol{f}_i$ are much larger than 5 N, the applied control forces $\Gamma(\boldsymbol{f}_i)$ are bounded by 5 N. The position and velocity tracking errors are shown in Fig. 8 and 9, respectively. It can be observed that the position and velocity tracking can be achieved in about 250 s, which is smaller than the prescribed time of 500 s. These results verify the effectiveness of the proposed controller 53.

The fuel required for the maneuver is related to the total velocity change ΔV_i, which is calculated by

$$\Delta V_i = \int_0^{t_f} \frac{\|\Gamma(\boldsymbol{f}_i)\|}{m_i} \mathrm{d}t, \ i = 1, \ldots, n. \tag{52}$$

where t_f is the convergence time. In this simulation, the values of velocity change of the four spacecraft are given in Table 3. The total velocity change ΔV of the four spacecraft is about 32.967 m/s and reasonable for practical space mission.

4.2. Comparison simulation

A comparison simulation is conducted between the proposed prescribed-time controller and a finite-time coordinated tracking controller (Eq. (17) in Hu and Zhang (2015)) in the revised manuscript. The finite-time coordinated tracking controller is defined as

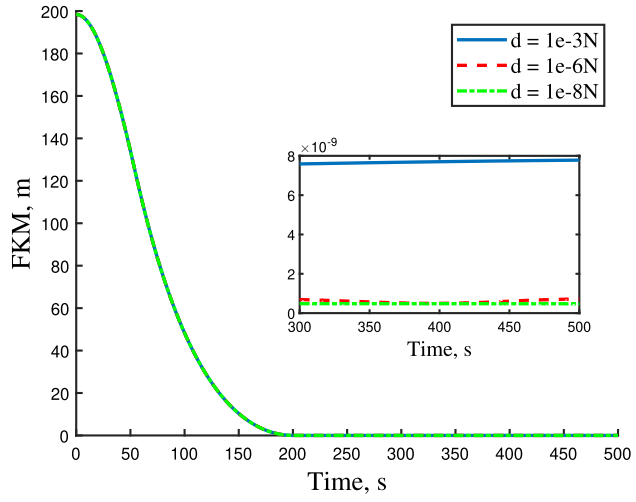

(a) FKM

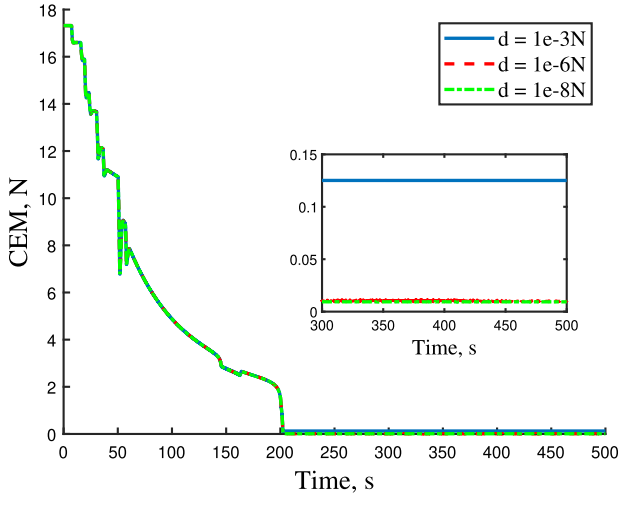

(b) CEM

Fig. 12. Performance comparison under proposed controller with 1^{-3}N, 1^{-6}N and 1^{-8}N external disturbances.

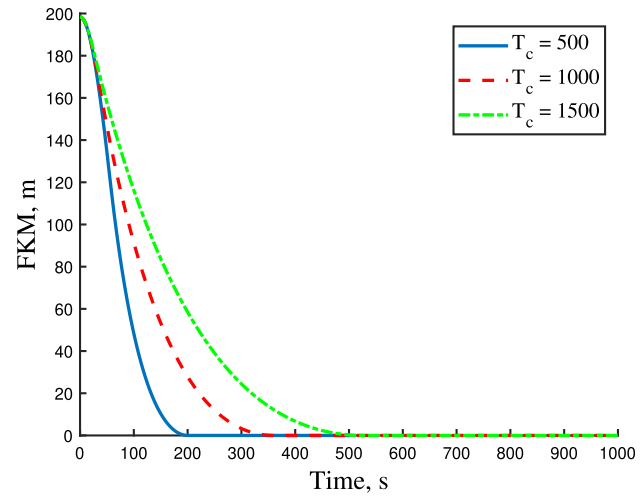

(a) FKM

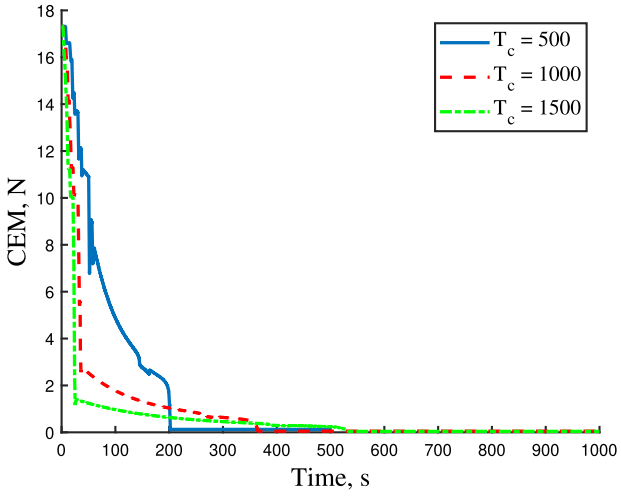

(b) CEM

Fig. 13. Performance comparison under proposed controller with $T_C = 500, T_C = 1000$ and $T_C = 1500$.

$$\begin{aligned} \boldsymbol{f}_i = \; & \boldsymbol{D}_i\rho_i + \boldsymbol{n}_i + \boldsymbol{M}_i\ddot{\rho}_d + \boldsymbol{C}_i\dot{\rho}_i \\ & -k_{pi}\left[\sum_{j=1}^{n} a_{ij}\mathrm{sig}(\rho_i-\rho_j)^{\alpha_1} + p_i\mathrm{sig}(\rho_i-\rho_d)^{\alpha_1}\right] \\ & -k_{di}\left[\sum_{j=1}^{n} a_{ij}\mathrm{sig}(\dot{\rho}_i-\dot{\rho}_j)^{\alpha_2} + d_i\mathrm{sig}(\dot{\rho}_i-\dot{\rho}_d)^{\alpha_2}\right] \end{aligned} \tag{53}$$

where $\boldsymbol{M}_i = m_i\boldsymbol{I}_3$, the control gains $\alpha_1, \alpha_2, k_{pi}, k_{di}, p_i$ and d_i are positive constants. In the comparison simulation, the control gains in (53) are chosen as $\alpha_1 = 0.5, \alpha_2 = 0.667$, and control gain are set as $k_{p1} = 0.01, k_{p2} = 0.01, k_{p3} = 0.01, k_{p4} = 0.01, k_{d1} = 0.1, k_{d2} = 0.1, k_{d3} = 0.1, k_{d4} = 0.1$, $p_1 = 10, p_2 = 10, p_3 = 10, p_4 = 10, d_1 = 10, \quad d_2 = 10, d_3 = 10, d_4 = 10$.

A formation-keeping error metric (FKM) and an overall control effort metric (CEM) are used to measure the performance of control scheme. SKM is defined as

$$\mathrm{FKM} = \frac{1}{n}\sqrt{\sum_{i=1}^{n}\|\chi_i\|^2} \tag{54}$$

CEM is defined as

$$\mathrm{CEM} = \sqrt{\sum_{i=1}^{n}\|\Gamma(\boldsymbol{f}_i)\|^2} \tag{55}$$

Fig. 10 shows the response curves of FKM and CEM of the two controllers. It can be found that the convergence rates under proposed prescribed-time controller are faster that those under the finite-time controller in (53).

We also conduct some simulation examples under the proposed prescribed-time controller with different parameters. The comparison results are shown in Fig. 11-Fig. 13. It can be observed from Fig. 11 that the stability of the proposed controller with the maximum allowable force can be guaranteed, but the convergence speed will decrease as the maximum allowable force decreases. As shown in Fig. 12, the steady-state FKM and CEM will increase as the disturbances increase. Finally, it can be observed from Fig. 13 that the parameter T_c affects deeply the convergence time of the control system. The convergence time is positively correlated with the parameter T_c.

5. Conclusion

In this paper, we study the prescribed-time relative motion coordinated control problem for spacecraft formation flying systems under input saturation. Based on the prescribed-time theory, a prescribed-time relative motion coordinated controller is proposed by using the prescribed-time sliding mode. We theoretically prove that the proposed controller the prescribed-time stability of SFF system. Furthermore, a simulation is carried out to verify the effectiveness of the proposed controller. The simulation results show that the spacecraft formation flying systems can achieve fast formation maneuvers with feasible fuel consumption and strong robustness under the proposed controller.

Declaration of Competing Interest

The authors declare that they have no known competing financial interests or personal relationships that could have appeared to influence the work reported in this paper.

Acknowledgments

This work was funded under the National Natural Science Foundation of China (61873312).

References

Anguiano-Gijón, C.A., Muñoz-Vázquez, A.J., Sánchez-Torres, J.D., et al., 2019. On predefined-time synchronisation of chaotic systems. Chaos, Solitons & Fractals 122, 172–178.

Chen, X., Yu, H., Hao, F., 2020. Prescribed-time event-triggered bipartite consensus of multiagent systems. IEEE Trans. Cybernet.
Chernick, M., D'Amico, S., 2021. Closed-form optimal impulsive control of spacecraft formations using reachable set theory. J. Guid., Control, Dynam. 44 (1), 25–44.
Di Mauro, G., Spiller, D., Rafano Carnà, S., et al., 2019. Minimum-fuel control strategy for spacecraft formation reconfiguration via finite-time maneuvers. J. Guid., Control, Dynam. 42 (4), 752–768.
Gurfil, P., 2005. Relative motion between elliptic orbits: generalized boundedness conditions and optimal formationkeeping. J. Guid., Control, Dynam. 28 (4), 761–767.
Hu, Q., Dong, H., Zhang, Y., et al., 2015. Tracking control of spacecraft formation flying with collision avoidance. Aerospace Sci. Technol. 42, 353–364.
Hu, Q., Shi, Y., 2020. Event-based coordinated control of spacecraft formation flying under limited communication. Nonlinear Dyn. 99 (3), 2139–2159.
Hu, Q., Zhang, J., 2015. Relative position finite-time coordinated tracking control of spacecraft formation without velocity measurements. ISA Trans. 54, 60–74.
Huang, Y., Jia, Y., 2019. Adaptive finite time distributed 6-dof synchronization control for spacecraft formation without velocity measurement. Nonlinear Dyn. 95 (3), 2275–2291.
Krastanov, M., 1995. Forward invariant sets, homogeneity and small-time local controllability. Banach Center Publications 32 (1), 287–300.
Lawson, P.R., 2001. The terrestrial planet finder. In: 2001 IEEE Aerospace Conference Proceedings (Cat. No. 01TH8542), pp. 4–2005. IEEE volume 4.
Lee, D., Sanyal, A.K., Butcher, E.A., 2015. Asymptotic tracking control for spacecraft formation flying with decentralized collision avoidance. J. Guid., Control, Dynam. 38 (4), 587–600.
Ma, Y., Zhang, K., Jiang, B., 2023. Prescribed-time fault-tolerant control for fully actuated heterogeneous multiagent systems: A hierarchical design approach. IEEE Trans. Aerospace Electron. Syst.
Ni, J.K., Liu, L., Liu, C.X., et al., 2017. Fixed-time leader-following consensus for second-order multiagent systems with input delay. IEEE Trans. Industr. Electron. 64 (11), 8635–8646.
Pini Gurfil, D.M., 2007. Cyclic spacecraft formations: relative motion control using line-of-sight measurements only. J. Guid. Control Dynam. 30 (1), 214–226.
Ran, D., Chen, X., Misra, A.K., 2017. Finite time coordinated formation control for spacecraft formation flying under directed communication topology. Acta Astronaut. 136, 125–136.
Rosen, P.A., Hensley, S., Joughin, I.R., et al., 2000. Synthetic aperture radar interferometry. Proc. IEEE 88 (3), 333–382.
Sánchez-Torres, J.D., Gómez-Gutiérrez, D., López, E., et al., 2018. A class of predefined-time stable dynamical systems. IMA J. Math. Control Inform/ 35 (Supplement_1), i1–i29.
Schaub, H., Alfriend, K.T., 2002. Hybrid cartesian and orbit element feedback law for formation flying spacecraft. J. Guid., Control, Dynam. 25 (2), 387–393.
Schaub, H., Vadali, S.R., Junkins, J.L., et al., 2000. Spacecraft formation flying control using mean orbit elements. J. Astronaut. Sci. 48 (1), 69–87.
Shang, Y., Ye, Y., 2017. Leader-follower fixed-time group consensus control of multiagent systems under directed topology. Complexity, 2017.
Sui, W.-S., Duan, G.-R., Hou, M.-Z., et al., 2019. Distributed fixed-time attitude synchronization control for multiple rigid spacecraft. Int. J. Control Autom. Syst. 17 (5), 1117–1130.
Sun, R., Wang, J., Zhang, D., et al., 2018. Neural-network-based sliding-mode adaptive control for spacecraft formation using aerodynamic forces. J. Guid., Control, Dynam. 41 (3), 757–763.
Wang, J., Liang, H., Sun, Z., et al., 2012. Finite-time control for spacecraft formation with dual-number-based description. J. Guid., Control, Dynam. 35 (3), 950–962.
Wang, Y., Song, Y., Hill, D.J., et al., 2018. Prescribed-time consensus and containment control of networked multiagent systems. IEEE Trans. Cybernet. 49 (4), 1138–1147.
Xiao, B., Wu, X., Cao, L., et al., 2021. Prescribed time attitude tracking control of spacecraft with arbitrary disturbance. IEEE Trans. Aerosp. Electron. Syst. 58 (3), 2531–2540.
Xie, S., Chen, Q., He, X., 2022. Predefined-time approximation-free attitude constraint control of rigid spacecraft. IEEE Trans. Aerosp. Electron. Syst. 59 (1), 347–358.
Xu, C., Wu, B., Wang, D., 2021a. Distributed prescribed-time attitude coordination for multiple spacecraft with actuator saturation under directed graph. IEEE Trans. Aerosp. Electron. Syst.
Xu, C., Wu, B., Zhang, Y., 2021b. Distributed prescribed-time attitude cooperative control for multiple spacecraft. Aerosp. Sci. Technol. 113, 106699.
Zhang, B.-Q., Song, S.-M., 2012. Decentralized coordinated control for multiple spacecraft formation maneuvers. Acta Astronaut. 74, 79–97.
Zhuang, M., Liguo, T., Kehang, L., et al., 2021a. Fixed-time position coordinated tracking control for spacecraft formation flying with collision avoidance. Chin. J. Aeronaut. 34 (11), 182–199.
Zhuang, M., Tan, L., Li, K., et al., 2021b. Fixed-time position coordinated tracking control for spacecraft formation flying with collision avoidance. Chin. J. Aeronaut. 34 (11), 182–199.
Zou, A.M., Fan, Z., 2020. Fixed-time attitude tracking control for rigid spacecraft without angular velocity measurements. IEEE Trans. Industr. Electron. 67 (99), 6795–6805.